Original Article

Polymer-wrapped reduced graphene oxide/nickel cobalt ferrite nanocomposites as tertiary hybrid supercapacitors: insights from experiment and simulation

K. Hareesh [a, d, *], Sachin R. Rondiya [b], Nelson Y. Dzade [b], S.D. Dhole [c], Jim Williams [d], Samarin Sergey [d]

[a] School of Applied Sciences (Physics), REVA University, Bengaluru 560064, India
[b] School of Chemistry, Cardiff University, Cardiff, CF10 3AT, Wales, United Kingdom
[c] Department of Physics, Savitribai Phule Pune University, Pune 411007, India
[d] School of Physics, University of Western Australia, Perth 6004, Australia

A B S T R A C T

The tertiary hybrid supercapacitor consisting of PEDOT:PSS wrapped reduced graphene oxide/$Ni_{0.5}Co_{0.5}Fe_2O_4$ (PGNC) was developed and its supercapacitance performance has been compared with that of the reduced graphene oxide (rGO)/$Ni_{0.5}Co_{0.5}Fe_2O_4$ (GNC), carbon nanotube (CNT)/$Ni_{0.5}Co_{0.5}Fe_2O_4$ (CNC) and carbon nanotube/reduced graphene oxide/$Ni_{0.5}Co_{0.5}Fe_2O_4$ (CGNC). Among all, PGNC exhibits an excellent specific capacitance of 1286 Fg^{-1} with a capacitance retention of 95% over 6000 cycles at a current density of 0.5 Ag^{-1}. The synergetic effects between rGO, $Ni_{0.5}Co_{0.5}Fe_2O_4$ and the PEDOT:PSS polymer result in an increase in the specific surface area and the pore volume, making PGNC an excellent hybrid supercapacitor for energy storage. The enhancement in the specific capacitance of the PGNC nanocomposite is further validated through first-principles density functional theory calculations, which predict an increment in the density of states at the Fermi level of the GNC and CNC nanocomposites compared to the isolated $Ni_{0.5}Co_{0.5}Fe_2O_4$ material. The supercapacitance performance of the PGNC nanocomposite is reported for different electrolytes, different stoichiometric ratios of Ni and Co in $Ni_xCo_{1-x}Fe_2O_4$ and on different substrates.

© 2021 The Authors. Publishing services by Elsevier B.V. on behalf of Vietnam National University, Hanoi. This is an open access article under the CC BY license (http://creativecommons.org/licenses/by/4.0/).

1. Introduction

Hybrid supercapacitors are the substitute energy storage devices towards the exhaustion of fossil fuels and related environmental issues due to their high power capability, fast charge–discharge ability and good stability for longer cycles [1]. Nevertheless, the technology is limited because of the low energy density [2]. Many attempts have been made to enhance the energy density of hybrid supercapacitors like developing coupled nanoparticles [3], coupling nanoparticles with conducting polymers [4], coupling nanoparticles with carbon nanotubes [5], scaffolding nanoparticles on reduced graphene oxide (rGO) sheets [6] *etc.*

Among all, the reduced graphene oxide (physical analog of graphene) based nanocomposites gained interest due to their good electrical conductivity and high specific surface area [7]. Also, rGO sheet avoids the agglomeration of scaffolded nanoparticles, thereby further increasing the specific surface area, as well as avoiding the dissolution of nanoparticles into the electrolyte during electrochemical performance [8–10].

Transition metal oxide nanoparticles such as RuO_2, MnO_2, $NiFe_2O_4$, NiO, $NiCo_2O_4$ *etc.* have been reported to be pseudo-capacitor electrode materials [11]. Nonetheless, the high toxicity and expensiveness of RuO_2 encumber its application in supercapacitors, whereas the relatively less electrical conductivity as well as specific capacitance of an individual transition metal oxide, makes it a candidate to improve their conductivity and specific capacitance [11]. Therefore, the binary transition metal oxide nanoparticles, for example, Ni/Mn oxide, Ni/Co oxide, Mn/Fe oxide, *etc.* have gained increased attention as they showed tremendous enhancement in electrochemical performance due to their ability to show different redox states [12]. Also, the ferrites

---

based on the binary transition metal such as $ABFe_2O_4$ (where A and B consist of combination of Mn, Cu, Ni, Co, etc.) based nanoparticles are expected to show enhanced supercapacitance behavior as they offer richer redox reactions due to the contributions from A, B and Fe ions than those of monometallic ferrites [13–15]. In this context, Bhujan et al. [13], have also found the specific capacitance of $CuCoFe_2O_4$ and $Al_{0.2}Cu_{0.4}Co_{0.4}Fe_2O_4$ as 397 Fg^{-1} and 548 Fg^{-1}, respectively at 100 mVs^{-1}. Bhujun et al. [14], have studied the pseudocapacitance behavior of $CuCoFe_2O_4$, $NiCoFe_2O_4$, $NiCuFe_2O_4$ and found the enhanced specific capacitance of 221 Fg^{-1}, 60 Fg^{-1}, 17 Fg^{-1} at 5 mVs^{-1}, respectively, compared to their respective monometallic ferrites. Elkholy et al. [15], have reported a specific capacitance of 675 Fg^{-1} at 1 mVs^{-1} for $MnCoFe_2O_4$, but the capacitance retention for this material was found decreased to 7.14% after 1000 cycles.

Among many mixed transition metal ferrites, $NiCoFe_2O_4$ nanoparticles are of great interest due to their well defined redox behavior, lower cost and environmental benignity. However, the application of this material in supercapacitors is hindered due to the agglomeration of the nanoparticles and the dissolution of the nanoparticles into electrolyte during the long operation. The agglomeration of nanoparticles can be avoided by scaffolding them on rGO sheets, thus, further increasing the surface area. The dissolution of nanoparticles into the electrolyte during long operation of the capacitor can be avoided by wrapping this binary, such as the $rGO/Ni_{0.5}Co_{0.5}Fe_2O_4$ nanocomposite using a suitable conducting polymer. Among many conducting polymers, Poly (3,4-ethyl-enedioxythiophene)-poly (styrenesulfonate) (from now on referred to as PEDOT:PSS), got significant attention for supercapacitor application due to its conjugated backbone and easy processability, thus, its ability to providing a fast path for the delocalization of electrons through the π orbitals. The oxygen atom in the PEDOT:PSS polymer has unfilled valence shells which act as doping level, making it a significant candidate for supercapacitance application [16]. The binary nanocomposites wrapped by PEDOT:PSS polymer leads to the availability of more active sites in terms of free volume/defects to store the charges and also it protects the dissolution of nanoparticles into electrolyte, which further increases the specific capacitance as well as the cyclic stability [17].

Therefore, in this work, the supercapacitor performances in terms of cyclic voltammetry (CV), charge–discharge (CD) and electrochemical impedance spectroscopy (EIS) of PEDOT:PSS/rGO/$Ni_{0.5}Co_{0.5}Fe_2O_4$ hybrid supercapacitor are reported. It is known that the specific capacitance of a hybrid supercapacitor is directly influenced by the presence of defects as well as the specific surface area. Positron annihilation lifetime spectroscopy (PALS) was used to gather information on defects and also the specific surface area was calculated using PALS parameters [18]. The obtained specific surface area of the hybrid supercapacitor was correlated with that measured from Brunauer–Emmett–Teller (BET) method. Further, first principles density functional theory calculations were used to validate the enhancement in supercapacitance of the PGNC nanocomposite. An attempt has also been made to compare the supercapacitance performance of the PGNC nanocomposite with that of the GNC, CGNC and CNC nanocomposites. The effect of the electrolytes, substrates and stoichiometric ratio of Ni and Co in PEDOT:PSS/rGO/$Ni_xCo_{1-x}Fe_2O_4$ on the specific capacitance of PGNC hybrid supercapacitor was also evaluated in this work.

2. Experimental

2.1. Materials

The outset materials such as sodium nitrate, sulfuric acid, graphite powder, potassium permanganate, hydrogen peroxide, lithium perchlorate, acetonitrile, nickel nitrate hydrate, cobalt nitrate hydrate, iron nitrate and urea were purchased from the Sigma Aldrich company. The multi-walled carbon nanotubes purchased from Global Nanotech (India) were mixed with nitric acid and heated for 6 h at 60 °C. The modified Hummer's method was used for the synthesis of the graphene oxide, and the detailed procedure has been described elsewhere [17].

2.2. Synthesis of nanocomposites

The ternary hybrid supercapacitor, PGNC, was synthesized as follows. 0.21 g of nickel nitrate hydrate, 0.21 g of cobalt nitrate hydrate, 1.21 g of iron nitrate hydrate and 1.79 g of urea were dissolved in 25 mL of distilled water. This aqueous solution was added dropwise in to 40 mL of GO (1 $mgmL^{-1}$) and stirred for half an hour. The resulting solution was refluxed at 100 °C in an oil bath for 11 h and, then 5 mL of PEDOT:PSS was mixed and the reflux reaction was processed for one more hour. Later, the refluxed solution was cooled to room temperature, centrifuged and dried at 60 °C for 12 h. Then, it was annealed at 350 °C for 3 h. The obtained product was named as PGNC. Similar procedure was followed for the synthesis of the CGNC sample by using 20 mL of GO (1 $mgmL^{-1}$) and 20 mL of CNTs (1 $mgmL^{-1}$). GNC and CNC samples were synthesized using 40 mL of GO (1 $mgmL^{-1}$) and 40 mL of CNTs (1 $mgmL^{-1}$) by keeping similar conditions same. The rGO and $Ni_{0.5}Co_{0.5}Fe_2O_4$ was synthesized under the similar conditions with nanoparticles precursors and GO, respectively.

2.3. Characterization and electrochemical studies

The synthesized nanocomposites were characterized by X-ray diffraction (XRD) using Bruker AXS D8 Advances with CuK$_\alpha$ source with scanning speed of 1°/min and step size of 0.01. Raman spectroscopy was carried out using the Renishaw Invia Raman microscope with the excitation wavelength of laser as 532 nm having a resolution of 1 μm with 5% of laser power. The spectral integration time was set as 20 s and four spectra were averaged resulting in exposure time of 80 s for each saved spectrum. The field emission scanning electron microscope (FESEM) of model Nova Nanosem 450 was used to record the surface morphology of all the samples. HRTEM images were obtained using the FEI Titan and JEOL 2100. Omicron EA 125 analyzer was used to perform X-ray photoelectron spectroscopy (XPS). 1 g of individual nanocomposite was used to measure the specific surface area and pore volume using Quantachrome, Model Autosorb iQ2 BET analyzer. Before the BET measurement, the nanocomposites were evacuated at 200 °C over night at 2 Pa vacuum. The presence of defects and free volume in nanocomposites were studied using PALS and its working principle is explained elsewhere [19]. The recorded PALS spectrum was resolved using PATFIT to get lifetime and intensity components.

The electrochemical performance such as CV, CD and EIS of all the samples were carried out using the SP 300, BioLogic potentiostat in Acetonitrile solution containing 1 M LiClO$_4$. The working electrode was prepared by mixing the active material, carbon black and PVDF with a weight ratio of 7:2:1 in NMP, and then loading resulting slurry on to carbon flag with a geometrical area of (1 × 1) cm^2. The coated flag samples were dried in a vacuum oven at 50 °C for 2 h. A three electrode system with platinum wire as the counter electrode, Ag wire as the reference electrode and active materials on carbon flag as the working electrode. To study the effect of the substrate (current collector), nickel foam was used along with carbon flag with the same geometrical area as mentioned above. The effect of the electrolyte on specific capacitance of the electrode material was studied using 1 M KCl, 1M NaCl and 1M LiClO$_4$ in acetonitrile. The prepared electrode material's specific capacitance (C_s) was determined using equations (1) and (2), respectively, by CV

and CD method. The coulombic efficiency (η), energy density (E_d) and power density (P_d) of the PGNC nanocomposite were calculated using equations (3)–(5), respectively [17,20].

$$C_s = \frac{2\int I(V)dV}{ms(V_1 - V_2)} \qquad (1)$$

$$C_s = \frac{i \cdot \Delta t_d}{m \cdot \Delta V} \qquad (2)$$

$$\eta = \frac{\Delta t_D}{\Delta t_C} \times 100\% \qquad (3)$$

$$E_d = 0.5 C_s (\Delta V)^2 \qquad (4)$$

$$P_d = \frac{E_d}{\Delta t_d} \qquad (5)$$

where $\int I(V)dV$ is area under CV curve, m is active mass of material on carbon flag, s is scan rate, (V_1–V_2) is working potential window in CV method, i is current density, Δt_d is discharge time, ΔV is voltage window in CD method and Δt_c is charging time.

2.4. Details of theoretical calculations

The theoretical calculations were done based on first-principles density functional theory (DFT) using the Vienna Ab initio Simulation Package [21,22]. The DFT code with periodic plane wave that includes the interaction between the valence and the core electrons using the Project Augmented Wave method [23] was used. The Perdew—Burke—Ernzerhof generalized gradient approximation functional method was used to calculate the electronic exchange—correlation potential [24]. An energy cut-off of 600 eV, and Monkhorst—Pack [25] k-point mesh of $5 \times 5 \times 5$ were used to sample the Brillouin zone of the bulk Ni$_{0.5}$Co$_{0.5}$Fe$_2$O$_4$. Geometry optimizations were performed using the conjugate-gradient algorithm until the residual Hellmann—Feynman forces on all relaxed atoms reached 10^{-3} eV Å^{-1}. To ensure an accurate description of the weak van der Waals interactions in the nanocomposites, the Grimme DFT-D3 dispersion correction scheme was employed, which adds a semi-empirical dispersion correction to the conventional Kohn—Sham DFT energy as implemented in the Vienna Ab initio Simulation Package code [26]. The Ni$_{0.5}$Co$_{0.5}$Fe$_2$O$_4$ (100) surface used for the formation of the rGO/Ni$_{0.5}$Co$_{0.5}$Fe$_2$O$_4$ and CNT/Ni$_{0.5}$Co$_{0.5}$Fe$_2$O$_4$ nanocomposites was created using the METADISE code [27], which ensures the creation of surfaces with zero dipole moment perpendicular to the surface plane. A vacuum size of 15 Å was added in the z-direction of the slab to circumvent the interactions among periodic slabs. The rGO/Ni$_{0.5}$Co$_{0.5}$Fe$_2$O$_4$ nano-heterostructure was constructed with the (4×4)-Ni$_{0.5}$Co$_{0.5}$Fe$_2$O$_4$ (100) and (5×5)-rGO supercells. Similarly, the CNT/Ni$_{0.5}$Co$_{0.5}$Fe$_2$O$_4$ nano-heterostructure was constructed with (4×4)-Ni$_{0.5}$Co$_{0.5}$Fe$_2$O$_4$ (100) and CNT with the diameter of 14.03 Å and the length of 10.88 Å.

3. Results and discussion

3.1. Characterization of hybrid supercapacitors

The structural properties of the synthesized hybrid nanocomposite was studied using XRD and results are depicted in Fig. S1 (a). The characteristic peaks of Ni$_{0.5}$Co$_{0.5}$Fe$_2$O$_4$ are observed at $2\theta = 29.97°$, $35.53°$, $43.12°$, $56.83°$ and $62.76°$, corresponding to the (220), (311), (400), (511) and (440) crystal planes, respectively, conforming the inverse spinel structure of Ni$_{0.5}$Co$_{0.5}$Fe$_2$O$_4$ [14] in CNC, CGNC and GNC nanocomposites. The obtained characteristic peaks of Ni$_{0.5}$Co$_{0.5}$Fe$_2$O$_4$ are in agreement with JCPDS file number 01-088-380. Nonetheless, PGNC showed the decrement in intensity of these peaks because of PEDOT:PSS polymer wrapping on Ni$_{0.5}$Co$_{0.5}$Fe$_2$O$_4$ nanoparticles. The broad peak around $2\theta = 25°$ in PGNC nanocomposite corresponds to the amorphous nature of PEDOT:PSS polymer [17]. The absence of the characteristic peak of rGO around $2\theta = 25°$ in CGNC and GNC nanocomposites was due to the exfoliation of rGO. As can be seen from Fig. S2 (a), the prepared rGO shows a peak around $2\theta = 24.5°$ corresponding to the (002) plane confirming the reduction of GO. Even, CNTs also showed a peak around $2\theta = 25°$ corresponding to the (002) plane confirming the presence of CNTs. Fig. S1 (b) depicts the comparison of the Raman spectra of the prepared nanocomposites. PGNC shows peaks around 1348 cm^{-1} corresponding to the D band, which arises due to the breathing mode of A$_{1g}$ phonons and at 1582 cm^{-1} corresponding to the G band, which arises due to the tangential vibrational mode of E$_{2g}$ phonons in sp^2 atoms. In addition to this, PGNC also shows a peak around 2682 cm^{-1} corresponding to 2D graphene [28]. The other nanocomposites, such as CNC, CGNC and GNC also exhibit the same kind of peaks, however, the wave number of both bands are shifted slightly due to the electron-phonon coupling. Apart from this, the ratio of the D band intensity to the G band intensity were found to be 1.09, 1.12, 1.24, 1.27 for CNC, CGNC, GNC and PGNC, respectively, indicating the reestablishment of the conjugated graphene network [28]. Fig. S2(b) displays the Raman spectra of rGO and CNTs. Fig. S3 (a-d) depicts the FESEM images of CNC, CGNC, GNC, PGNC nanocomposites, respectively. As can be seen from Figs. S3(a) and S3(b), the diameter of the CNTs are found to be in the range of 14 nm—20 nm. The decoration of the Ni$_{0.5}$Co$_{0.5}$Fe$_2$O$_4$ nanoparticles with size of around (15—40) nm on CNTs, rGO sheets and CNTs/rGO has been observed in CNC, CGNC and GNC nanocomposites, respectively. The rGO was found to be smooth as well as homogeneous as can be seen from its TEM image from Fig. S3(e). Nonetheless, PGNC nanocomposite showed a thin layer of PEDOT:PSS polymer wrapping on Ni$_{0.5}$Co$_{0.5}$Fe$_2$O$_4$/rGO. The HRTEM of GNC nanocomposite is shown in Fig. S3(f), which shows the d-spacing (distance between two layers) as 2.97 Å. This resembles to the (311) plane of Ni$_{0.5}$Co$_{0.5}$Fe$_2$O$_4$ nanoparticle corroborating the XRD results. Fig. S4 shows the elemental mapping of GNC nanocomposites. It is worth noting that the elements, such as Ni, Co, Fe, C and O are homogeneously distributed throughout the GNC nanocomposite. XPS was used to study the quantitative analysis of elemental composition. The XPS survey scan of the PGNC sample in the binding energy range from 100 eV to 1000 eV is depicted in Fig. S5. The C1s XPS spectra of GO is displayed in Fig. S6(a). The main peak of C1s was deconvoluted into four different peaks at 284.4 eV, 285.8 eV and 286.9 eV corresponding to C=C, C—O and C=O, respectively. Nevertheless, the intensity of the C—O and C=O groups is decreased in C1s of PGNC nanocomposite (shown in Fig. S6(b)) indicating the removal of these groups, which in turn confirm the formation of rGO [11]. Fig. S6(c) depicts the Ni 2P XPS spectra of PGNC, exhibiting doublet peak at 856.06 eV and 865.09 eV, respectively, which are attributed to Ni 2P$_{3/2}$ and Ni 2P$_{1/2}$. The Co 2P XPS spectra of PGNC displayed in Fig. S6(d), depicts peaks around 780.1 eV and 797.2 eV representing Co 2P$_{3/2}$ and Co 2P$_{1/2}$, respectively. The XPS spectra of Fe 2P is displayed in Fig. S6(e) with two peaks at 711.46 eV and 725.12 eV corresponding to Fe 2P$_{3/2}$ and Fe 2P$_{1/2}$, respectively. The doublet peak of S 2P as shown in Fig. S6(f) reveals the existence of the two components, such as S 2P$_{3/2}$ and S 2P$_{1/2}$ with the binding energy as 162.4 eV and 163.6 eV, respectively [16]. Table T1 summarizes the surface structural features, such as the specific surface area and the pore volume of the

nanocomposites. The corresponding nitrogen adsorption–desorption isotherms are depicted in Fig. S7, which shows the hysteresis loop of type IV indicating the more distributed meso-porosity in the nanocomposites [29]. It can be seen from Table T1, that the CNC nanocomposite exhibits a specific surface area of 221 $m^2 g^{-1}$ and it is enhanced to 272 $m^2 g^{-1}$ for the PGNC nano-composite. In addition to this, even the pore volume measured by BET analysis was also enhanced from 0.37 $cm^3 g^{-1}$ for CNC nano-composite to 0.91 $cm^3 g^{-1}$ for PGNC nanocomposite. The enhanced specific surface area and pore volume of PGNC nanocomposite compared to other nanocomposites reveals that the PGNC provides more active sites for the charge storage leading to the enhancement in the supercapacitance performance of the PGNC nanocomposite. The obtained PALS spectrum was resolved to get three lifetime components τ_1, τ_2 and τ_3 with the intensities I_1, I_2 and I_3,

respectively, and the results are tabulated in Table T2. The GO was reduced to rGO during nanocomposite synthesis, so the rGO in all nanocomposites has defects in it. The lifetime component τ_1, infer the sum of the lifetime of bulk positron and the residence time of Bloch state [30]. Nonetheless, the lifetime component τ_2 along with the corresponding intensity I_2 reveals the presence of large defect characteristics. The intensity I_2 is found to be as large as 72.6718% for the PGNC composite compared to other nanocomposites indi-cating a high concentration of free volume defects/vacancies in it. Further, this also reveals the significant trapping of positrons in these defects/vacancies. In addition to this, the τ_2 value found to be less ($\tau_2 = 327$ ps) for the PGNC nanocomposite indicating the enrichment of free volume defects which arises due to PEDOT:PSS wrapping. Furthermore, the *in-situ* reduction of GO to rGO during nanocomposite synthesis also contributes to the generation of
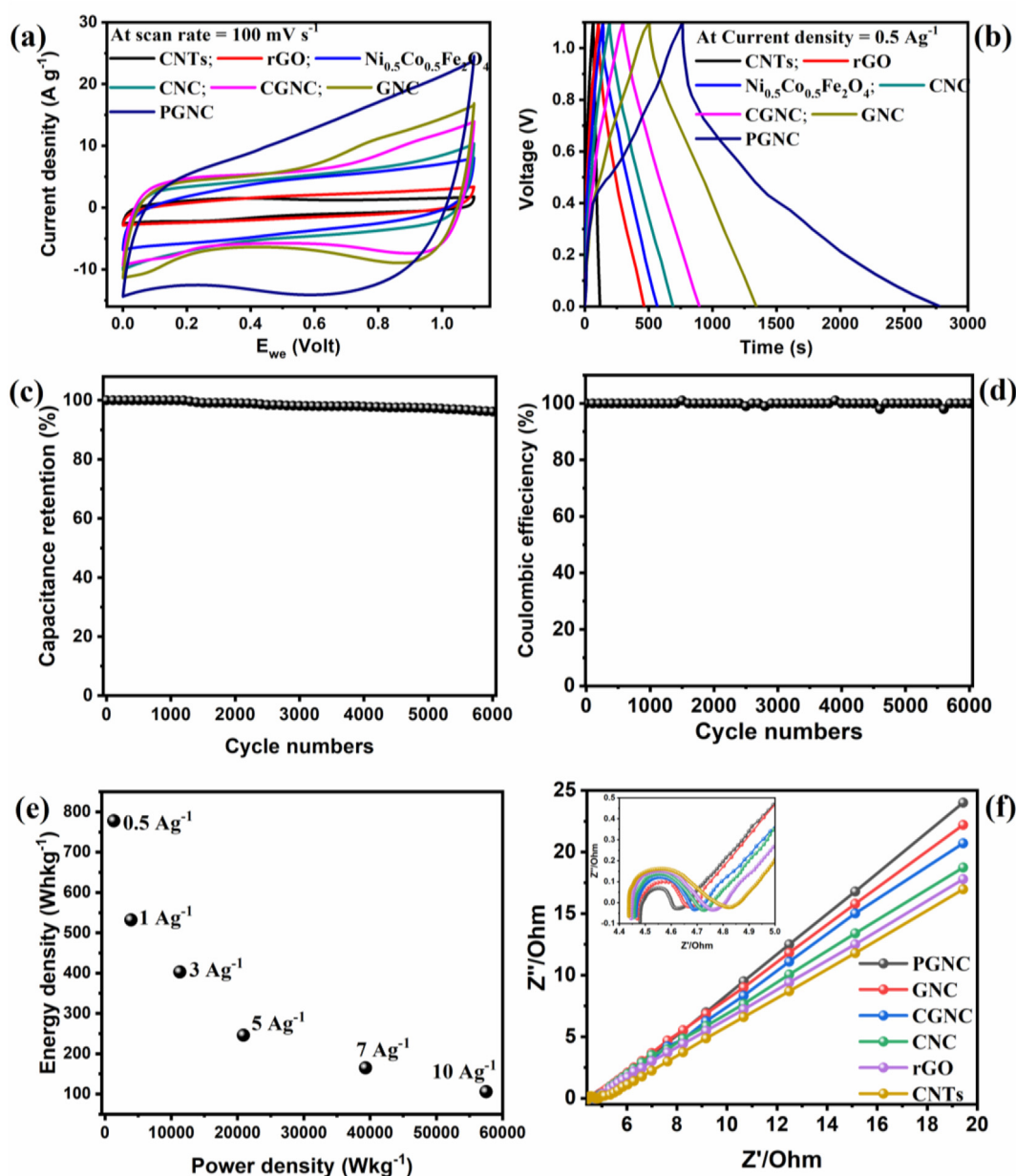

Fig. 1. (a) Cyclic Voltagrams and (b) Charge–Discharge curves of different nanocomposites; (c) Capacitance retention, (d) Coulombic efficiency and (e) Ragone plot of PGNC nanocomposite; (f) Nyquist plots for different nanocomposites (Inset of Fig. 1(f) shows the enlarged view at higher frequencies).

vacancies in the nanocomposites. Table T2 also tabulates the third lifetime component τ_3, which represents the o-Ps atom formation in defects (free volume) or vacancies of nanocomposites. The obtained τ_3 values was found to be 1553.9 ps for CNTs and 1995.8 ps for PGNC nanocomposites. The increase in τ_3 value for PGNC nanocomposite indicates the enhancement in the free volume defects/vacancies. The intensity I_3 increases significantly from 6.399% for CNTs to 12.636% for the PGNC nanocomposite signifying the enhancement in the specific surface area of nanocomposites [18]. The specific surface area of nanocomposites was calculated using I_3 by the formula [18],

$$I_3 = 3.0 + 0.033S \tag{6}$$

where S is the specific surface area. The Table T2 lists the values of the specific surface area calculated using the above equation. It is observed from the table that the specific surface area was found to be 105 m^2 g^{-1} for CNTs and 292 m^2 g^{-1} for PGNC nanocomposite, which is in consistence with the BET analysis results. The larger specific surface area of the PGNC nanocomposite suggests more storage of charges in it. The fractional free volume (f in %) was calculated using the formula [30],

$$f = AV_f I_3 \tag{7}$$

where $V_f = \frac{4}{3}\pi R^3$ is the size of free volume defects, R is the radius of free volume defects and A (=1) is a constant. It is interesting to observe that PGNC exhibits the highest free volume fraction (1.22%) revealing the greater number of defects (free volume) in it, supporting the aforementioned explanation.

3.2. Electrochemical performance of hybrid supercapacitors

The electrochemical properties, such as CV, CD and EIS of the nanocomposites were studied using the three electrode system. The CV curves in the potential interval of 0−1.1 V for hybrid supercapacitors along with rGO and CNTs are presented in Fig. 1(a). Among all CV curves of the samples, the one for the PGNC nanocomposite exhibits the semi rectangular shape suggesting the pseudocapacitive behavior [31]. It is also worthy to mention that the area of CV curve for PGNC nanocomposite more likely suggests a large supercapacitance of it. The C_s values for all the electrode materials were determined using equation (1) and are listed in Table 1. It is observed from Table 1 that the PGNC shows higher specific capacitance of 1164 Fg^{-1} due to its large specific surface area as studied from BET and PALS analysis in previous sections. Fig. S8(a) depicts the CV curve for PGNC electrode materials at various scan rates and all of them exhibit an increment in the current density with the scan rate. Even at 100 mVs^{-1}, the PGNC nanocomposite shows the highest specific capacitance of 198 Fg^{-1} as depicted in Table T3. The in-situ reduction of GO to rGO enhances

the fast electronic charge transfer pathways which result in the more intensive diffusion of Li$^+$ (from electrolyte). The diffusion coefficient of Li$^+$ ions (D) was calculated using the relation between the maximum current (i_p in A) and scan rate (v) represented by [32],

$$i_p = 2.69 \times 10^5 n^{3/2} A D^{1/2} C v^{1/2} \tag{8}$$

where 'n' is the number of electrons involved in the oxidation, 'A' is the active electrode area, 'C' is the Li$^+$ concentration. The D values determined using equation (8) are found as 0.89×10^{-11} cm^2 s^{-1}, 1.24×10^{-11} cm^2 s^{-1}, 1.47×10^{-11} cm^2 s^{-1} and 1.93×10^{-11} cm^2 s^{-1} respectively, for the CNC, CGNC, GNC and PGNC electrode materials. The D value was found to be larger for the PGNC nanocomposite being attributed to the good distribution of particles and the enhanced conductivity between PEDOT:PSS, rGO and Ni$_{0.5}$Co$_{0.5}$Fe$_2$O$_4$ results in the enhanced supercapacitance performance [33].
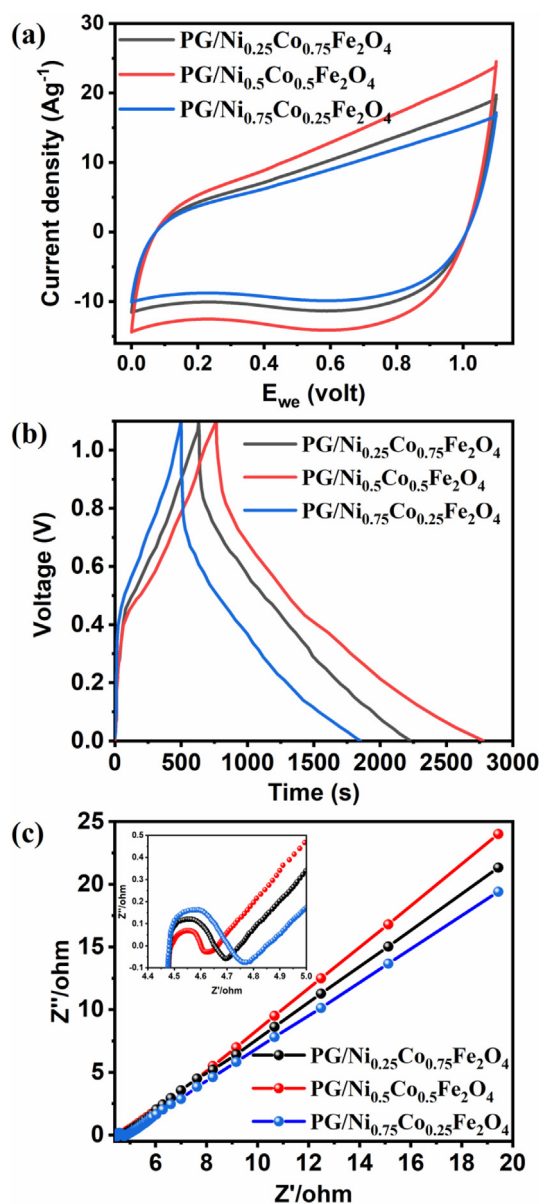
Fig. 2. (a) Cyclic Voltagrams, (b) Charge−Discharge curves and (c) Nyquist plots of PG/Ni$_x$Co$_{1-x}$Fe$_2$O$_4$ nanocomposites.

Table 1
Specific capacitance values of different nanocomposites found by using CV (at 5 mVs^{-1}) and CD (at 0.5 Ag^{-1}) method.

Material	Specific capacitance (Fg^{-1})	
	CV method	CD method
CNTs	73	78
rGO	206	230
Ni$_{0.5}$Co$_{0.5}$Fe$_2$O$_4$	254	270
CNC	301	316
CGNC	337	384
GNC	512	534
PGNC	1164	1286

Furthermore, the specific capacitance of all the nanocomposites was calculated using the reliable galvanostatic charge−discharge technique with equation (2). The CD curves at 0.5 A $\cdot$g^{-1} for all the samples are depicted in Fig. 1(b). All samples exhibit a symmetrical shape of the charge−discharge curves (except for the PGNC nanocomposite) suggesting the electric double layer capacitance behavior. Nevertheless, PGNC electrode material depicts a deviation from the symmetrical CD curves owing to its pseudocapacitance behavior as explained in the previous section and also the discharge time was found to be longer for the PGNC nanocomposite indicating that it has greater specific capacitance values. The calculated values of specific capacitance for the different nanocomposites are listed in Table 1. Interestingly, PGNC nanocomposite shows higher specific capacitance value of 1286 Fg^{-1} at 0.5 Ag^{-1} compared to all other nanocomposites. This is attributable to synergetic effects between rGO, Ni$_{0.5}$Co$_{0.5}$Fe$_2$O$_4$ and PEDOT:PSS as follows: (i) the scaffolding of Ni$_{0.5}$Co$_{0.5}$Fe$_2$O$_4$ nanoparticle on the rGO sheet limits its restacking leading to the enhancement in the specific surface area as supported by BET as well as PALS analysis, this in turn causes increasing the electrolyte/electrode contact area. Also, Ni and Co in the nanoparticle form enhance the redox potential as well as the specific capacitance, (ii) the *in-situ* reduction of GO to rGO creates vacancies/defects and the addition of PEDOT:PSS polymer provide more active sites for the efficient storage of charges, (iii) the addition of PEDOT:PSS polymer may also limit the aggregation and dissolution of the nanoparticles into the electrolyte, thereby enhancing the specific capacitance of the PGNC nanocomposite. The CD curves of the PGNC nanocomposite at different current densities are shown in Fig. S8(b) and the obtained specific capacitance values are presented in Table T3. Even at 10 A g^{-1}, the specific capacitance of the PGNC nanocomposite was found to be 175 Fg^{-1}. The calculated C_S of PGNC electrode material is compared with those reported in the literature in Table T4.

The capacitance retention is the most vital parameter of the electrode material for its practical application. The study of the long term cyclic stability of the PGNC nanocomposite at the maximum voltage of 1.1 V was carried out at 0.5 Ag^{-1} over 6000 cycles and the results are displayed in Fig. 1(c). The PGNC nanocomposite shows an excellent stable capacitance retention of 94% due to the stabilizing behavior of PEDOT:PSS that helps to retain the nanoparticle structure and also to prevent the nanoparticles for dissolving into the electrolyte during CD process and thus, providing excellent capacitance retention. The another important performance parameter for the quantification as the electrode material is the coulombic efficiency revealing the amount of charges involved in the device which facilitate the electrochemical reaction [17]. The calculated coulombic efficiency (using equation (3)) for the PGNC hybrid supercapacitor is displayed in Fig. 1(d), which depicts the same value for 6000 cycles without any variation revealing the lower energy dissipation. The Ragone plot, displayed in Fig. 1(e), depicts the energy density E_d and power density P_d of the hybrid supercapacitor as 1320 W h$\cdot$kg^{-1} and 778 Wkg^{-1}, respectively, at 0.5 Ag^{-1}. It is noteworthy to observe that the E_d descends with the increase in P_d, which is consistent with literature reports [17,31].

The resistive and capacitive behavior of the hybrid supercapacitor was studied using EIS and the corresponding Nyquist plots are displayed in Fig. 1(f). The plot exhibits straight line behavior in the lower frequencies region and semicircle behavior in the range of higher frequencies. The semicircle represents the faradaic reaction and its diameter represents the interfacial transfer resistance [6]. It can be observed from Fig. 1(f) that PGNC nanocomposite shows the lowest semicircle indicating the lower internal resistance and the reduced interfacial transfer resistance, making it appropriate as a supercapacitor. Further, the impedance spectra was analysed using Randel circuit. As it is shown in Fig. S9,

the circuit consists of an internal resistance (R_i), the electrical double layer capacitance (C_L), the interfacial transfer resistance (R_{ct}) and the Warburg impedance (W_z). The results derived are listed in Table T5. It is observed that the PGNC nanocomposite shows smaller values of R_i and R_{ct} indicating the reduced internal resistance and low interfacial transfer resistance, revealing PGNC a good electrode material for the hybrid supercapacitor. Since the PGNC nanocomposite exhibited an enhanced specific capacitance compared to those of CNC, CGNC and GNC, it is considered for further electrochemical characterization experiments.

3.3. Electrochemical characterization of PEDOT:PSS/rGO/Ni$_x$Co$_{1-x}$Fe$_2$O$_4$

The stoichiometry ratio of Ni and Co in PEDOT:PSS/rGO/Ni$_x$Co$_{1-x}$Fe$_2$O$_4$ (PG/Ni$_x$Co$_{1-x}$Fe$_2$O$_4$) shall affect its specific capacitance value. Therefore, the electrochemical characterization experiments, such
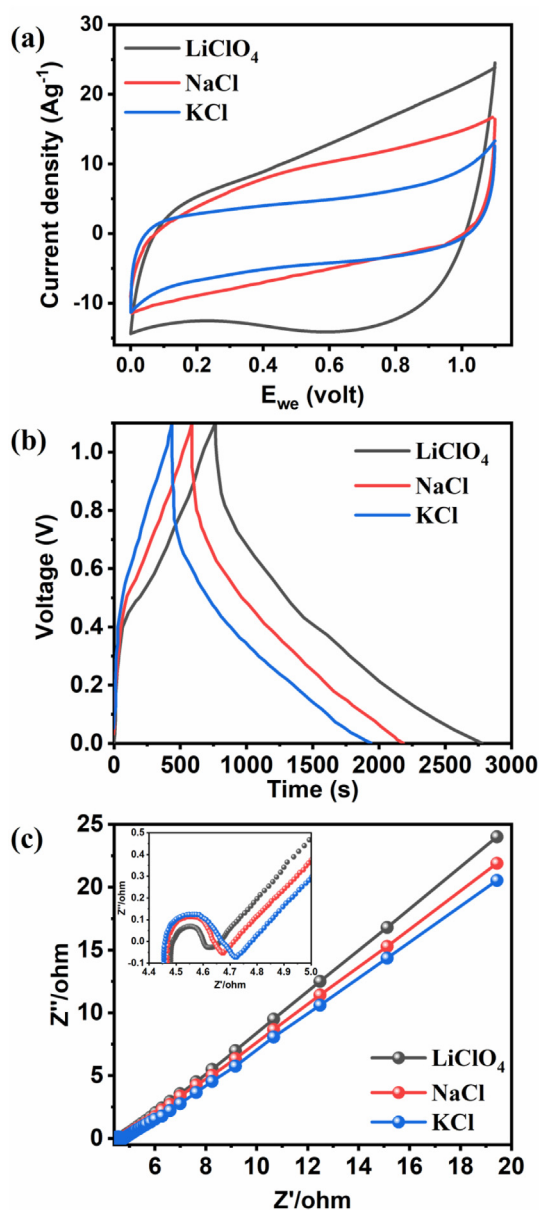

Fig. 3. (a) Cyclic Voltagrams, (b) Charge−Discharge curves and (c) Nyquist plots of PGNC electrode material in different electrolytes.
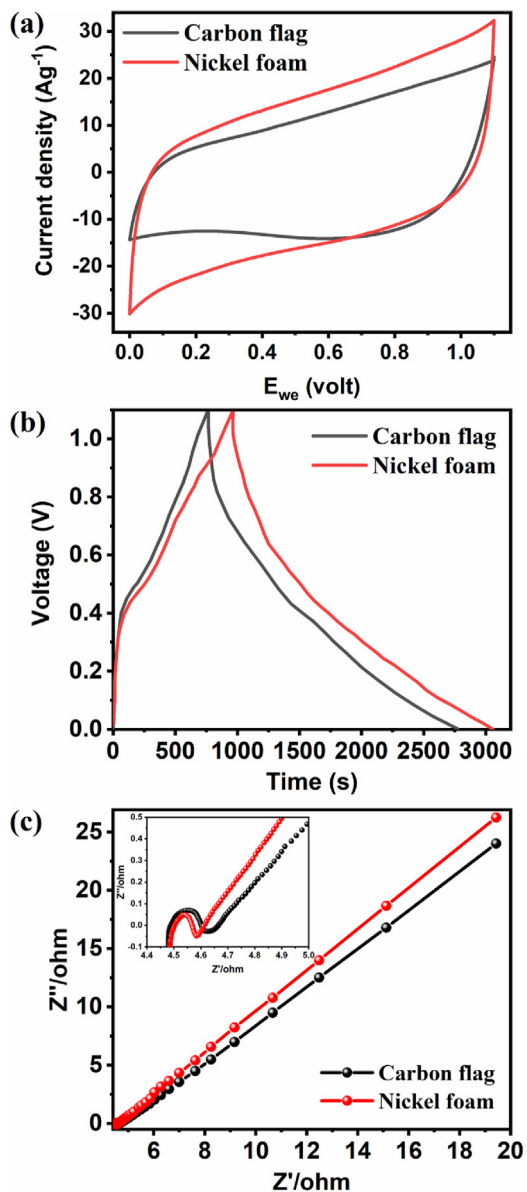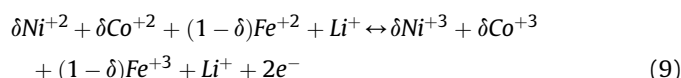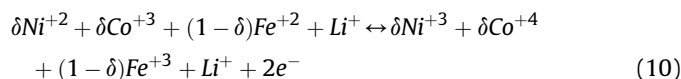
Fig. 4. (a) Cyclic Voltagrams, (b) Charge−Discharge curves and (c) Nyquist plots of PGNC nanocomposite on different substrates.

as CV, CD and EIS were carried out in 1M LiClO$_4$ dissolved in Acetonitrile solution. Fig. 2(a) displays the CV curves of the PEDOT:PSS/rGO/Ni$_x$Co$_{1-x}$Fe$_2$O$_4$, where x = 0.25, 0.5 and 0.75 at 100 mVs^{-1}. It can be seen from Fig. 2(a) that the area under the CV curves varies as PG/Ni$_{0.25}$Co$_{0.75}$Fe$_2$O$_4$ < PG/Ni$_{0.5}$Co$_{0.5}$Fe$_2$O$_4$ > PG/Ni$_{0.75}$Co$_{0.25}$Fe$_2$O$_4$ suggesting the greater specific capacitance from PG/Ni$_{0.5}$Co$_{0.5}$Fe$_2$O$_4$ to be due to the equal contribution from Ni and Co ions. It is also noteworthy to observe that the area under the CV curves for PG/Ni$_{0.25}$Co$_{0.75}$Fe$_2$O$_4$ is more likely compared to the ones of PG/Ni$_{0.75}$Co$_{0.25}$Fe$_2$O$_4$ suggesting a greater specific capacitance of PG/Ni$_{0.25}$Co$_{0.75}$Fe$_2$O$_4$. In order to calculate the specific capacitance of PG/Ni$_x$Co$_{1-x}$Fe$_2$O$_4$, the CD was carried out at 0.5 Ag^{-1} and the result is depicted in Fig. 2(b). All the CD curves of PG/Ni$_x$Co$_{1-x}$Fe$_2$O$_4$ (x = 0.25, 0.5 and 0.75) exhibit a pseudocapacitive behavior. The calculated specific capacitance is found as 1017 Fg^{-1}, 1286 Fg^{-1}, and 865 Fg^{-1}, respectively, for PG/Ni$_{0.25}$Co$_{0.75}$Fe$_2$O$_4$, PG/Ni$_{0.5}$Co$_{0.5}$Fe$_2$O$_4$ and PG/Ni$_{0.75}$Co$_{0.25}$Fe$_2$O$_4$. The larger specific capacitance of PG/Ni$_{0.5}$Co$_{0.5}$Fe$_2$O$_4$ is due to the equal contribution from Ni and Co towards the electrochemical reaction, which can be described as follows:

$$\delta Ni^{+2} + \delta Co^{+2} + (1-\delta)Fe^{+2} + Li^+ \leftrightarrow \delta Ni^{+3} + \delta Co^{+3}$$
$$+ (1-\delta)Fe^{+3} + Li^+ + 2e^- \qquad (9)$$

and

$$\delta Ni^{+2} + \delta Co^{+3} + (1-\delta)Fe^{+2} + Li^+ \leftrightarrow \delta Ni^{+3} + \delta Co^{+4}$$
$$+ (1-\delta)Fe^{+3} + Li^+ + 2e^- \qquad (10)$$

In the PG/Ni$_{0.5}$Co$_{0.5}$Fe$_2$O$_4$ nanocomposite, Ni and Co may exists as Ni^{+2}, Co^{+2} and Co^{+3} resulting in a larger number of ions for the exchange at the electrode−electrolyte interface, which in turn results in a greater storage of charges revealing the greater specific capacitance. It can also be observed that the PG/Ni$_{0.25}$Co$_{0.75}$Fe$_2$O$_4$ shows a greater specific capacitance compared to the PG/Ni$_{0.75}$Co$_{0.25}$Fe$_2$O$_4$ due to the larger number of Co ions in the electrochemical reaction leading to a greater value of C_s. Fig. 2(c) shows the Nyquist plots for the PEDOT:PSS/rGO/Ni$_x$Co$_{1-x}$Fe$_2$O$_4$ composite. It can be observed that the PEDOT:PSS/rGO/Ni$_{0.5}$Co$_{0.5}$Fe$_2$O$_4$ displays the lowest semicircle, indicating its lower internal resistance. This, together with the low interfacial transfer resistance, enables the more ion exchanges leading to its enhanced specific capacitance, which is also supporting the CV and CD results.
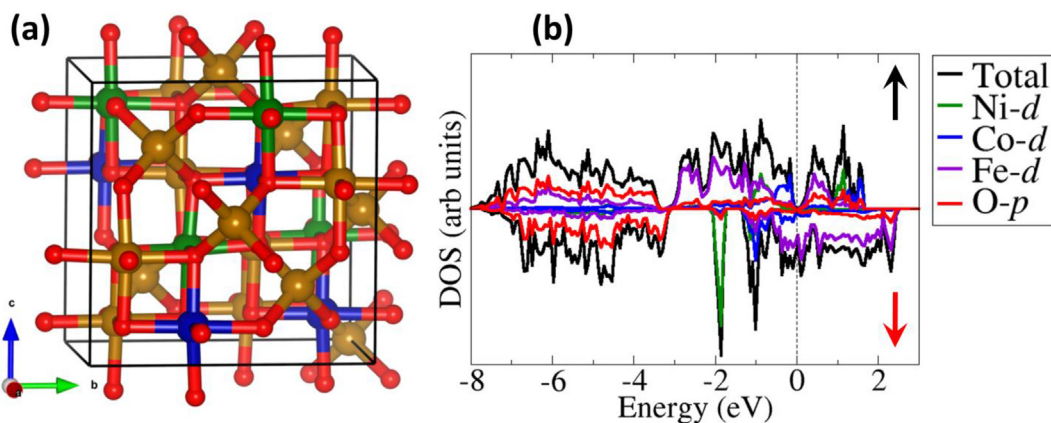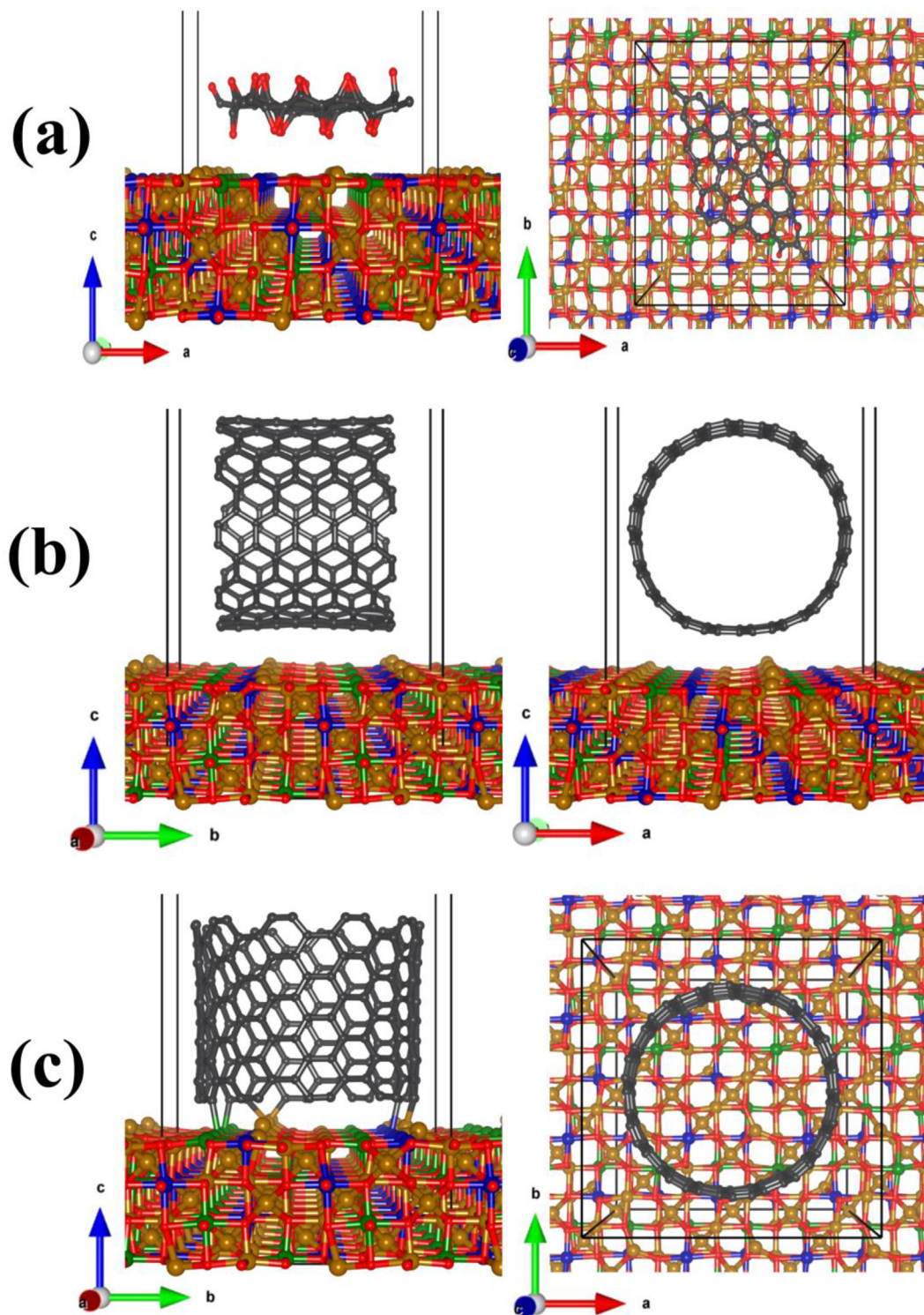

Fig. 5. (a) The cubic structure (b) the partial density of states (PDOS) of bulk Ni$_{0.5}$Co$_{0.5}$Fe$_2$O$_4$. The tetrahedral Fe ions have spin up ordering whereas the octahedral ones including the Ni and Co ions have spin down ordering, giving a ferromagnetic inverse spinel structure.

Fig. 6. Schematic representation of the optimized heterostructures of (a) rGO/Ni$_{0.5}$Co$_{0.5}$Fe$_2$O$_4$, (b) H-CNT/Ni$_{0.5}$Co$_{0.5}$Fe$_2$O$_4$ and (c) V-CNT/Ni$_{0.5}$Co$_{0.5}$Fe$_2$O$_4$. H-CNT and V-CNT denote horizontal and vertical mode of carbon nanotube heterojunction with Ni$_{0.5}$Co$_{0.5}$Fe$_2$O$_4$ surface.

3.4. Effect of electrolyte on the specific capacitance of PGNC nanocomposite

The specific capacitance of the electrode material is strongly influenced by the electrolyte used because of the difference in the cationic radius, conductivity and their exchange at the electrode–electrolyte interface [34]. Fig. 3(a) depicts the CV of the PGNC nanocomposite carried out in 1 M KCl, 1 M NaCl and 1 M LiClO$_4$ at 100 mV s^{-1}. As can be seen from Fig. 3(a), the area under the CV curves varies in the order LiClO$_4$ > NaCl > KCl demonstrating the greatest specific capacitance of the PGNC electrode in LiClO$_4$ which is due to the smaller ionic radius of Li$^+$ (0.59 Å) compared to those of Na$^+$

(1.02 Å) and K$^+$ (1.38 Å), leading to more intense diffusion of the Li$^+$ ions [35]. The specific capacitance of the PGNC electrode in 1M KCl, 1M NaCl and 1M LiClO$_4$ were calculated using CD curves as displayed in Fig. 3(b). All CD curves exhibit asymmetrical shape and the discharge time decreases in the order LiClO$_4$ > NaCl > KCl indicating the greater specific capacitance of the PGNC nanocomposite for 1M LiClO$_4$. The calculated specific capacitance of the PGNC nanocomposite was found as 1286 Fg^{-1}, 1021 Fg^{-1}, and 961 Fg^{-1}, respectively, in 1M LiClO$_4$, 1M NaCl and 1M KCl. The greater specific capacitance of the PGNC electrode material in 1M LiClO$_4$, which can be attributed to the smaller ionic radius of Li$^+$ causing more intensive diffusion of the inserted/de-inserted Li$^+$ ions that further facilitates the Faraday reaction. Fig. 3(c) shows the Nyquist plots of the PGNC nanocomposite obtained with different electrolytes. It is found that the PGNC nanocomposite shows a smaller semicircle for 1M LiClO$_4$ compared to 1M NaCl and 1M KCl. This supports also the afore-mentioned CV and CD results.

3.5. Effect of substrate on the specific capacitance of PGNC nanocomposite

The substrate (here as the current collector) used in the electrochemical characterization also plays an important role in storing the charges in turn the specific capacitance of electrode material [36]. Fig. 4(a) depicts the CV curves of the PGNC nanocomposite taken in 1M LiClO$_4$ in acetonitrile using carbon flag and nickel foam. The Fig. 4(a) shows the higher current for Ni foam compared to carbon flag due to its high specific surface area, more porosity and fast electron-ion transport [36,37], which leads to stronger adsorption of the electrolyte ions and faster exchange of the ions at the electrode–electrolyte interface. These in turn lead to a larger specific capacitance of the PGNC electrode material on the Ni foam substrate. The CD curves of the PGNC nanocomposite with carbon flag and Ni foam as the substrate are displayed in Fig. 4(b). The specific capacitance of PGNC was found to be 1286 Fg^{-1} and 1349 Fg^{-1} for the carbon flag and Ni foam substrate, respectively. As the Ni foam demonstrates a larger specific surface area and a high porosity, resulting in the adsorption of more Li$^+$ ions from the electrolyte and in the enhancement of the contact surface area of

PGNC. In addition to this, the good conductivity of Ni foam boosts the faster electron/ion exchange at the electrolyte–electrode interface. The above mentioned synergistic effects of Ni foam and PGNC nanocomposite enhance the specific capacitance. The Nyquist plots of PGNC nanocomposite with carbon flag and Ni foam substrate are displayed in Fig. 4(c). As can be seen from this figure, the PGNC with the Ni foam substrate exhibits smaller semicircles compared to that with the carbon flag substrate. This indicates a smaller internal resistance, which in turn reveals the good conductivity. Further, the smaller semicircle of the PGNC nanocomposite with the Ni foam substrate also indicates the low interfacial transfer resistance making the more intensive ion exchange between the electrode and the electrolyte corroborating the aforementioned CV and CD results.

3.6. First-principles DFT simulations

The electronic structures (density of states) of rGO/Ni$_{0.5}$Co$_{0.5}$Fe$_2$O$_4$ and CNT/Ni$_{0.5}$Co$_{0.5}$Fe$_2$O$_4$ nanocomposites, which dictates the quantum capacitance of a material, were determined using first-principles DFT calculations to corroborate the obtained enhancement in the supercapacitance performance. The bulk Ni$_{0.5}$Co$_{0.5}$Fe$_2$O$_4$ was modelled in the cubic inverse spinel structure with the space group $Fd\overline{3}m$, which is shown in Fig. 5(a). The lattice parameter from a full geometry optimization is predicted at 8.302 Å in close agreement with known experimental estimates [38,39]. The inverse spinel Ni$_{0.5}$Co$_{0.5}$Fe$_2$O$_4$ structure is characterized by one half of the octahedral sites being occupied by the Co^{2+} and Ni^{2+} cations and the other half of the octahedral sites as well as all of the tetrahedral sites being occupied by the Fe^{3+} cations. The partial density of states (PDOS) of the bulk Ni$_{0.5}$Co$_{0.5}$Fe$_2$O$_4$ is shown in Fig. 5(b), which reveals a nearly half-metallic characteristics, with the magnetic moment of the tetrahedral and octahedral Fe^{3+} ions predicted at 3.45 and 3.62 μ_B. The Co and Ni ions, on the other hand, have the magnetic moments of 2.32 and 1.34 μ_B, respectively.

The Ni$_{0.5}$Co$_{0.5}$Fe$_2$O$_4$ (100) crystal plane was considered for the formation of the rGO/Ni$_{0.5}$Co$_{0.5}$Fe$_2$O$_4$ and CNT/Ni$_{0.5}$Co$_{0.5}$Fe$_2$O$_4$
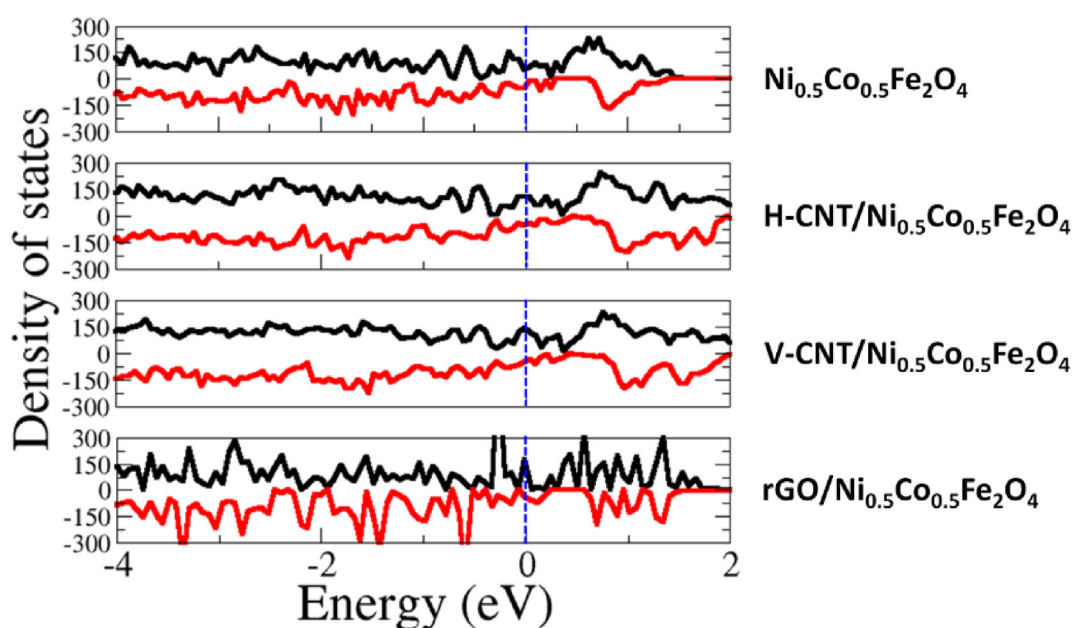

Fig. 7. Density of states (DOS) for pristine Ni$_{0.5}$Co$_{0.5}$Fe$_2$O$_4$, H-CNT/Ni$_{0.5}$Co$_{0.5}$Fe$_2$O$_4$, V-CNT/Ni$_{0.5}$Co$_{0.5}$Fe$_2$O$_4$ and rGO/Ni$_{0.5}$Co$_{0.5}$Fe$_2$O$_4$ heterostructures. H-CNT and V-CNT denote horizontal and vertical mode of carbon nanotube heterojunction with Ni$_{0.5}$Co$_{0.5}$Fe$_2$O$_4$ surface. DOS of spin up (black) and spin down (red).

nanocomposites because it does not contain any dangling bonds and established in the lowest surface energy. Shown in Fig. 6 is the optimized structure of the rGO/$Ni_{0.5}Co_{0.5}Fe_2O_4$ (Fig. 6(a)) and CNT/$Ni_{0.5}Co_{0.5}Fe_2O_4$ (Fig. 6b, c) nanocomposites. For the CNT/$Ni_{0.5}Co_{0.5}Fe_2O_4$ heterostructure, the carbon nanotube was oriented in the horizontal (Fig. 6(b)) and vertical (Fig. 6(c)) geometries. The closest O−Fe, O−Co and O−Ni bond distances at the rGO/$Ni_{0.5}Co_{0.5}Fe_2O_4$ interface are calculated to be 2.74, 2.98, and 3.16 Å, respectively, indicating weak interactions between the rGO monolayers. The horizontal CNT geometry is also found to interact weakly with the $Ni_{0.5}Co_{0.5}Fe_2O_4$ (100) surface, with the closest C−Fe, C−Ni, and C−Co bonds, predicted at 3.01, 3.63, and 3.72 Å, respectively. The vertical geometry on the other hand forms strong C−Fe (2.01 Å), C−Ni (2.22 Å), and C−Co (2.31 Å) bonds releasing stronger interface adhesion energy. The interfacial adhesion energy, calculated as $E_{ad} = (E_{A/B} - (E_A + E_B))/S$, where $E_{A/B}$, E_A and E_B are the total energy of the nanocomposite with interface surface area S, the individual ground state relaxed total energy of A and B surfaces, respectively, was used to assess the thermodynamic stability of the formed heterojunctions. The adhesion energy of the rGO/$Ni_{0.5}Co_{0.5}Fe_2O_4$ interface is predicted at -0.09 eV $Å^{-2}$, whereas for the CNT/$Ni_{0.5}Co_{0.5}Fe_2O_4$ interface with the CNT in horizontal and vertical geometries it was calculated to yield -0.13 and -0.22 eV $Å^{-2}$, respectively. The predicted negative interfacial adhesion energies indicate that the rGO/$Ni_{0.5}Co_{0.5}Fe_2O_4$ and CNT/$Ni_{0.5}Co_{0.5}Fe_2O_4$ nanocomposites are thermodynamically stable.

Considering that the density of states (DOS) at the Fermi level, dictates the quantum capacitance of a material, with the higher DOS giving rise to an enhanced capacitance. We have determined the DOS of the naked $Ni_{0.5}Co_{0.5}Fe_2O_4$ surface and compared it with that of the rGO/$Ni_{0.5}Co_{0.5}Fe_2O_4$ and CNT/$Ni_{0.5}Co_{0.5}Fe_2O_4$ nanocomposites and the results are depicted in Fig. 7. The figure shows that the rGO/$Ni_{0.5}Co_{0.5}Fe_2O_4$ hybrid nanocomposites have higher DOS at the Fermi level compared to the isolated $Ni_{0.5}Co_{0.5}Fe_2O_4$ surface. The enhancement in DOS due to the coupling of $Ni_{0.5}Co_{0.5}Fe_2O_4$ with rGO and CNT is thus suggested as the primary origin for the observed enhanced supercapacitance of the hybrid nanocomposites. A previous DFT-based simulations by Lenz et al. [40], showed that the PEDOT:PSS systems has electronic densities of states (DOS) at the Fermi level. Therefore, the wrapping of PEDOT:PSS on rGO/$Ni_{0.5}Co_{0.5}Fe_2O_4$ is expected to enhance the DOS and hence the specific capacitance of the PGNC nanocomposite, which also corroborate the experimental results.

4. Conclusion

The hybrid PEDOT:PSS wrapped rGO/$Ni_{0.5}Co_{0.5}Fe_2O_4$ supercapacitors were successfully synthesized and demonstrated to exhibit the enhanced supercapacitance performance as compared to NGC, GCN and CNC nanocomposites. The enhancement in the supercapacitance performance of the PGNC hybrid supercapacitor was attributed to the synergetic effect between the individual components, in which PEDOT:PSS and rGO offer many active sites as well as provide supporting layers for the $Ni_{0.5}Co_{0.5}Fe_2O_4$ nanoparticles, restricting them from aggregation and dissolution. These effects result in an increased specific surface area, which is also supported by the BET and PALS measurements. The increased specific capacitance of the PGNC nanocomposite was further supported by theoretical calculations, which showed the enhancement of the DOS at the Fermi level due to the coupling with rGO and hence the observed enhanced supercapacitance of the PGNC nanocomposite. The effects of the electrolytes and the substrate materials on the supercapacitance performance of PGNC electrode material were also studied.

Declaration of competing interest

The authors declare that they have no known competing financial interests or personal relationships that could have appeared to influence the work reported in this paper.

Appendix A. Supplementary data

Supplementary data to this article can be found online at https://doi.org/10.1016/j.jsamd.2021.03.001.

References

[1] A. Afif, S.M.H. Rahman, A.T. Azad, J. Zaini, M.A. Islan, A.K. Azad, Advanced materials and technologies for hybrid supercapacitors for energy storage − a review, J. Energy storage 25 (2019) 100852.

[2] A. Gonzalez, E. Goikolea, J.A. Barrena, R. Mysyk, Review on supercapacitors: technologies and materials, Renew. Sustain. Energy Rev. 58 (2016) 1189−1206.

[3] Y. Yang, K. Shen, Y. Liu, Y. Tan, X. Zhao, J. Wu, et al., Novel hybrid nanoparticles of vanadium nitride/porous carbon as an anode material for symmetrical supercapacitor, Nano-Micro Lett. 9 (2017) 6.

[4] H.M. Shiri, A. Ehsani, M.J. Khales, Electrochemical synthesis of Sm_2O_3 nanoparticles: application in conductive polymer composite films for supercapacitors, J. Colloid Interface Sci. 505 (2017) 940−946.

[5] L. Li, Z.A. Hu, N. An, Y.Y. Yang, Z.M. Li, H.Y. Wu, Facile Synthesis of MnO_2/CNTs composite for supercapacitor electrodes with long cycle stability, J. Phys. Chem. C 118 (2014) 22865−22872.

[6] K. Hareesh, B. Shateesh, R.P. Joshi, J.F. Williams, D.M. Phase, S.K. Haram, et al., Ultra high stable supercapacitance performance of conducting polymer coated MnO_2 nanorods/rGO nanocomposites, RSC Adv. 7 (2017) 20027−20036.

[7] S.K. Tiwari, S. Sahoo, N. Wang, A. Huczko, Graphene research and their outputs: status and prospect, J. Sci.: Adv. Mat. And Devices 5 (2020) 10−29.

[8] W.H. Low, S.S. Lim, C.H. Chia, C.W. Siong, P.S. Khiew, Three-dimensional lion's mane like AlV_3O_9 deposited on graphene surface for supercapacitors with a promising electrochemical performance, J. Sci.: Adv. Mat. And Devices 5 (2020) 164−172.

[9] S. Ranganatha, N. Munichandraiah, γ-MnS nanoparticles anchored reduced graphene oxide: electrode materials for high performance supercapacitors, J. Sci.: Adv. Mat. And Devices 3 (2018) 359−365.

[10] M. Saranya, R. Ramachandran, F. Wang, Graphene-zinc oxide (G-ZnO) nanocomposite for electrochemical supercapacitor applications, J. Sci.: Adv. Mat. And Devices 1 (2016) 454−460.

[11] C. An, Y. Zhang, H. Guo, Y. Wang, Metal oxide-based supercapacitors: progress and prospectives, Nanoscale Adv 1 (2019) 4644−4658.

[12] S.-K. Chang, K.-T. Lee, Z. Zainal, K.-B. Tan, N.A. Yusof, W.M.D.W. Yusoff, et al., Structural and electrochemical properties of manganese substituted nickel cobaltite for supercapacitor application, Electrochim. Acta 67 (2012) 67−72.

[13] B. Bhujun, M.T.T. Tan, A.S. Shanmugam, Evaluation of aluminium doped spinel ferrite electrodes for supercapacitors, Ceram. Int. 42 (2016) 6457−6466.

[14] B. Bhujun, M.T.T. Tan, A.S. Shanmugam, Study of mixed ternary transition metal ferrites as potential electrodes for supercapacitor applications, Results in Physics 7 (2017) 345−353.

[15] A.E. Elkholy, F.E.-T. Heakal, N.K. Allam, Nanostructured spinel manganese cobalt ferrite for high-performance supercapacitors, RSC Adv. 7 (2017) 51888−51895.

[16] T. Cheng, Y.Z. Zhang, J.D. Zhang, W.Y. Lai, W. Huang, High-performance free standing PEDOT:PSS electrodes for flexible and transparent all-solid-state supercapacitors, J. Mater. Chem. 4 (2016) 10493−10499.

[17] K. Hareesh, B. Shateesh, R.P. Joshi, S.S. Dahiwale, V.N. Bhoraskar, S.K. Haram, et al., PEDOT:PSS wrapped $NiFe_2O_4$/rGO tertiary nanocomposite for the supercapacitor applications, Electrochim. Acta 201 (2016) 106–116.

[18] K. Venkateswaran, K.L. Cheng, Y.C. Jean, Application of positron annihilation to study the surface properties of porous resins, J. Phys. Chem. 88 (1984) 2465–2469.

[19] K. Hareesh, D.V. Sunitha, P. Ramya, J.F. Williams, S. Samarin, S.D. Dhole, et al., Gamma radiation-assisted diffusion of Au nanoparticles in nanocavities of polycarbonate: nano-structural and surface properties, Mater. Res. Express 5 (2018), 015304.

[20] R. Samal, B. Chakraborty, M. Saxena, D.J. Late, C.S. Rout, Facile production of mesoporous WO_3-rGO hybrids for high-performance supercapacitor electrodes: an experimental and computational study, ACS Sustain. Chem. Eng. 7 (2019) 2350–2359.

[21] G. Kresse, J. Hafner, Theory of the crystal structures of selenium and tellurium: the effect of generalized-gradient corrections to the local-density approximation, Phys. Rev. B 50 (1994) 13181–13185.

[22] G. Kresse, D. Joubert, From ultrasoft pseudopotentials to the projector augmented-wave method, Phys. Rev. B 59 (1999) 1758–1775.

[23] P.E. Blöchl, Projector augmented-wave method, Phys. Rev. B 50 (1994) 17953–17979.

[24] J.P. Perdew, K. Burke, M. Ernzerh, Generalized gradient approximation made simple, Phys. Rev. Lett. 78 (1997) 1396.

[25] H.J. Monkhorst, J.D. Pack, Special points for Brillouin-zone integrations, Phys. Rev. B 13 (1976) 5188.

[26] S. Grimme, J. Antony, S. Ehrlich, H. Krieg, A consistent and accurate ab initio parametrization of density functional dispersion correction (DFT-D) for the 94 elements H-Pu, J. Chem. Phys. 132 (2010) 154104.

[27] G.W. Watson, E.T. Kelsey, N.H. de Leeuw, D.J. Harris, S.C. Parker, Atomistic simulation of dislocations, surfaces and interfaces in MgO, Chem. Soc. Faraday Trans. 92 (1996) 433–438.

[28] L.M. Malard, M.A. Pimenta, G. Dresselhaus, M.S. Dresselhaus, Raman spectroscopy in graphene, Phys. Rep. 473 (2009) 51–87.

[29] M. Elkady, H.S. Hassan, A. Hashim, Immobilization of magnetic nanoparticles onto amine-modified nano-silica gel for copper ions remediation, Materials 9 (2016) 460.

[30] U. Rana, M.G. Nambissan, S. Malika, K. Chakrabarti, Effects of process parameters on the defects in graphene oxide-polyaniline composites investigated by positron annihilation spectroscopy, Phys. Chem. Chem. Phys. 16 (2014) 3292–3298.

[31] P. Krishnaiah, B.P. Prasanna, K.Y. Kumar, P.K. Asha, P. Nautiyal, V.S.A. Devi, F.A. Alharthi, L. Parashuram, M.S. Rahu, Fabrication of anode material for asymmetric supercapacitor device using polyaniline wrapped boroncarbonitride nanocomposite with enhanced capacitance, J. Alloys Compd. 848 (2020) 156602.

[32] N. Ding, J. Xu, Y.X. Yao, G. Wegner, X. Fang, C.H. Chen, et al., Determination of the diffusion coefficient of lithium ions in nano-Si, Solid State Ionics 180 (2009) 222–225.

[33] L.L. Zhang, S. Duan, X.L. Yang, G. Peng, G. Liang, Y.H. Huang, et al., Reduced graphene oxide modified Li_2FeSiO_4/C composite with enhanced electrochemical performance as cathode material for lithium ion batteries, Appl. Mater. Inter. 3 (2015) 12304–12309.

[34] B. Pal, S. Yang, S. Ramesh, V. Thangadurai, R. Jose, Electrolyte selection for supercapacitive devices: a critical review, Nanoscale Adv 1 (2019) 3807–3835.

[35] J. Zhu, Y. Xu, J. Wang, J. Lin, X. Sun, S. Mao, The effect of various electrolyte cations on electrochemical performance of polypyrrole/RGO based supercapacitors, Phys. Chem. Chem. Phys. 17 (2015) 28666–28673.

[36] R. Awata, M. Shehab, A.E. Tahan, M. Soliman, S. Ebrahim, High performance supercapacitor based on camphor sulfonic acid doped polyaniline/multiwall carbon nanotubes nanocomposite, Electrochim. Acta 347 (2020) 136229.

[37] Y. Liu, X. Zhang, K.M. Postolek, P. Yang, Ni_2P nanosheets modified N-doped hollow carbon spheres towards enhanced supercapacitor performance, J. Alloys Compd. 854 (2021) 157111.

[38] M.A. Almessiere, Y. Slimani, M. Sertkol, M. Nawaz, A. Sadaqat, A. Baykal, et al., Effect of Nb^{3+} substitution on the structural, magnetic and optical properties of $Co_{0.5}Ni_{0.5}Fe_2O_4$ nanoparticles, Nanomaterials 9 (2019) 430.

[39] M.K. Kokare, N.A. Jadhav, Y. Kumar, K.M. Jadhav, S.M. Rathod, Effect of Nd^{3+} doping on structural and magnetic properties of $Ni_{0.5}Co_{0.5}Fe_2O_4$ nanocrystalline ferrites synthesized by sol-gel auto combustion method, J. Alloys Compd. 748 (2018) 1053–1061.

[40] A. Lenz, H. Kariis, A. Pohl, P. Persson, L. Ojamäe, The electronic structure and reflectivity of PEDOT:PSS from density functional theory, Chem. Phys. 384 (2011) 44–51.